

Evidence for Proportionate Partition Between the Magnetic Field and Hot Gas in Turbulent Cassiopeia A

Jonathan W. Keohane¹, E. V. Gotthelf² and R. Petre³

*The Laboratory for High Energy Astrophysics
Code 662, Goddard Space Flight Center
Greenbelt, MD 20771*

Accepted by ApJ Letters 5/1/98

ABSTRACT

We present a deep X-ray observation of the young Galactic supernova remnant Cas A, acquired with the ROSAT High Resolution Imager. This high dynamic range (232 ks) image reveals low-surface-brightness X-ray structure, which appears qualitatively similar to corresponding radio features. We consider the correlation between the X-ray and radio morphologies and its physical implications. After correcting for the inhomogeneous absorption across the remnant, we performed a point by point (4'' resolution) surface brightness comparison between the X-ray and radio images. We find a strong ($r = 0.75$) log-log correlation, implying an overall relationship of $\log(\Sigma_{\text{x-ray}}) \propto (2.21 \pm 0.05) \times \log(\Sigma_{\text{radio}})$. This is consistent with proportionate partition (and possibly equipartition) between the local magnetic field and the hot gas — implying that Cas A's plasma is fully turbulent and continuously amplifying the magnetic field.

Subject headings: supernova remnants – supernovae: individual (Cas A) — X-rays: ISM — turbulence — MHD — techniques: image processing

¹The University of Minnesota; E-mail: jonathan@lheamail.gsfc.nasa.gov

²Universities Space Research Association; E-mail: gotthelf@gsfc.nasa.gov

³E-mail: petre@lheavx.gsfc.nasa.gov

1. Introduction

A comparison of the X-ray and radio emission of young supernova remnants (SNRs) provides a powerful tool for investigating the physical relationships among the thermal plasma, cosmic ray electrons and the magnetic field (e.g., Dickel et al. 1982; Matsui et al. 1984; Arendt et al. 1990; Dyer & Reynolds 1998). Radio emission is governed primarily by the density of relativistic electrons and the magnetic field strength, while the intensity in soft X-rays is dictated by the gas density. Shell SNRs provide excellent laboratories for investigating the interaction among these physical processes, with Cas A being the natural launching point for such investigations, because of its high surface brightness in both the radio and X-ray wavelength regimes.

Previous work has shown that the soft X-ray morphology of Cas A, on angular scales $\gtrsim 30''$ (or 0.5 pc at a distance of 3.4 kpc), is dominated by absorption effects (Keohane, Rudnick, & Anderson 1996, hereafter KRA). When this absorption is taken into account, a higher degree of intrinsic correlation between the X-ray and radio images is found. Similarly, Holt et al. (1994) found a correlation between the radio and the hard X-ray ($E > 4.5$ keV) surface brightness, which is not affected by absorption. These correlations demonstrate that a simple relationship may exist among the underlying physical parameters.

In this Letter we investigate the relationship between the radio and X-ray emission on smaller angular scales. We use a newly acquired ROSAT High Resolution Imager (HRI) image of Cas A, with a 40 times longer exposure than used in KRA. To account for the inhomogeneous column density towards Cas A, we “deabsorb” the image using H I and OH absorption data (§2.2). We perform a point by point ($4''$ resolution) surface brightness comparison between the X-ray and radio images and find a statistically significant correlation (§2.3). We discuss the physical implications of this correlation (§3) and its implications for future observational and theoretical studies of Cas A and other young SNRs (§4).

2. Analysis

2.1. The Deep ROSAT Image of Cas A

Deep ROSAT HRI exposures of the SNR Cas A were obtained on December 23, 1995 and June 20, 1996, with the telescope optical axis pointed toward

the center of the remnant. The standard processing yields a total of 232 ks of acceptable observing time, which produces the highest dynamic range (500:1) X-ray image of Cas A to date. A final image, shown in Fig. 1, was made by cross-correlating and adding images from the two exposures, using the radio image as an absolute reference.

In order to reduce instrumental blurring (e.g. the HRI “halo”) we applied 5 iterations of the Lucy-Richardson restoration technique (Richardson 1972; Lucy 1974). As a kernel for the deconvolution, we used an on-axis analytical radially symmetric point spread function (PSF), which is valid because the PSF is approximately constant across the $5'$ extent of Cas A. The resolution of the final image was estimated to be about $4''$ (0.07 pc).

To correct any systematic scaling errors that may have been produced by the restoration process, we used a $4''$ FWHM Gaussian smoothed version of the raw image to rescale the reconstructed image. This required a linear transformation with a scale of 0.92 and an insignificant zero-offset (0.31 cts/beam).

This new image of Cas A is the first with enough sensitivity to reveal X-ray features, on small angular scales ($\theta \gtrsim 4''$) and low surface brightness ($\Sigma_{\text{HRI}} \gtrsim 0.03 \text{ cts s}^{-1} (')^{-2}$), which have been only previously detected in the radio. Many of the most striking of these features are outside the bright shell, such as the northern and southern knots and the eastern jet region. To enhance this outlying structure, we show a spatially filtered version of the image (Fig. 3), produced by dividing the $4''$ X-ray image by a $60''$ Gaussian smoothed version of itself. This effectively removes large scale structure and enhances regions away from the bright ring.

2.2. The Deabsorbed Image

The large scale differences between Cas A’s soft X-ray and radio morphology are dominated by foreground absorption effects (KRA). In order to take these effects into account, we used H I and OH absorption data (Schwarz, Goss, & Kalberla 1997; Bieging & Crutcher 1986), which trace the foreground atomic and molecular gas respectively. We translated these data into an optical depth map using the empirical relation (specific to Cas A) for each resolution element:

$$\tau_x = 0.073 \text{ km}^{-1} \text{ s} \times EW_{\text{H I}} + 1.6 \text{ km}^{-1} \text{ s} \times EW_{\text{OH}} + 1.6 \quad (1)$$

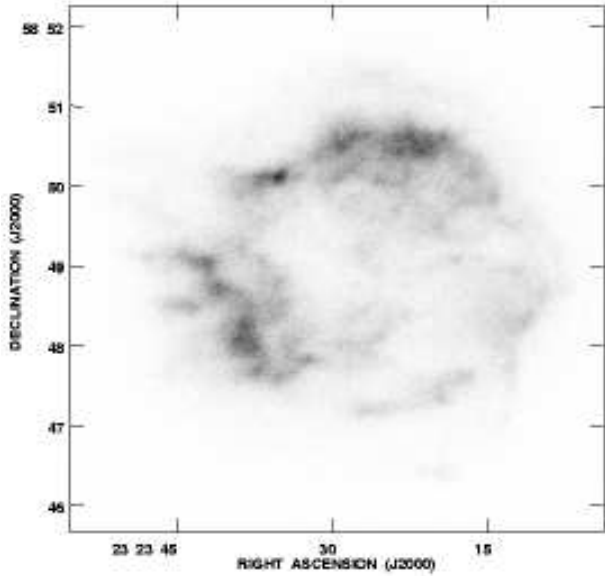


Fig. 1.— The 232 ks ROSAT HRI raw image scaled linearly. The maximum value is $102 \frac{\text{counts}}{0.5'' \text{ pixel}}$. This image is oversampled with a pixel size of $0.5''$.

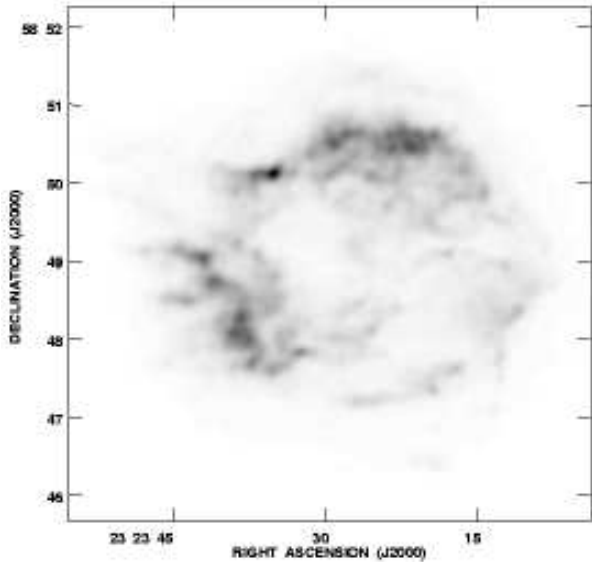


Fig. 2.— The Lucy-Richardson deconvolved image with $4''$ resolution. This greyscale is scaled linearly with a maximum value of $5300 \frac{\text{counts}}{4'' \text{ beam}}$. This image is oversampled with a $0.5''$ pixel size, but has a resolution of $4''$.

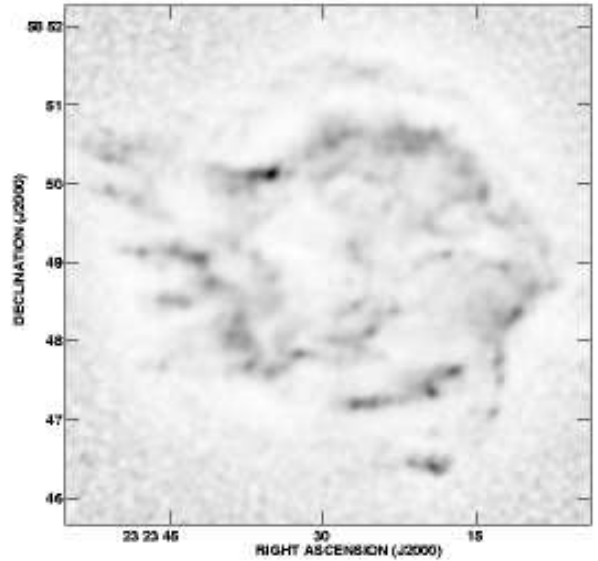


Fig. 3.— The deconvolved ROSAT HRI image divided by a $60''$ smoothed version of itself. This figure is included in order to show the outlying and small scale structure revealed by this deep exposure.

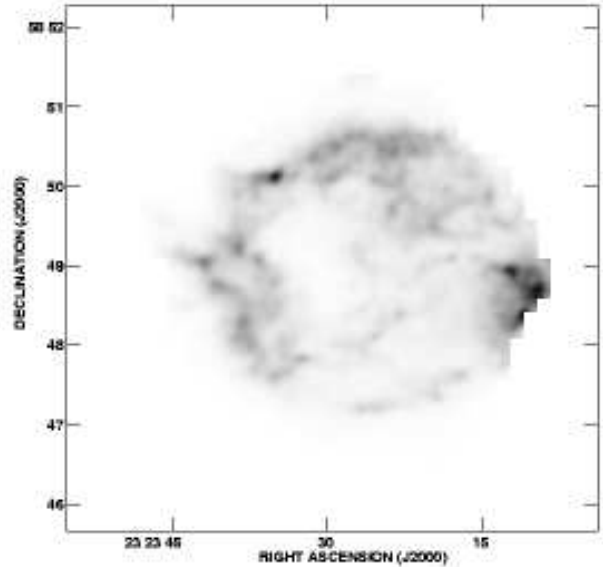


Fig. 4.— The deabsorbed ROSAT image scaled linearly. This image is oversampled with a $0.5''$ pixel size, but its resolution is $4''$. Note that the intervening column density was mapped in absorption, so this image is blanked outside of Cas A's radio-bright disk where the H I and OH optical depths are unreliable.

where τ_x is Cas A’s optical depth over the ROSAT HRI bandpass, and $EW_{\text{H I}}$ and EW_{OH} are the H I and OH equivalent widths respectively. A complete description of this method is given in KRA.

Using this HRI-specific 30'' resolution optical depth map, we produced the deabsorbed X-ray image of Cas A shown in Fig. 4. Absorption structure on scales between 30'' and 4'' could affect our results, but the OH data of Biegging & Crutcher suggest that clouds of scales 30''–60'' dominate the absorption structure.

2.3. A Comparison with the Radio Image

The brightest features in the X-ray and radio maps are for the most part not correlated. However, when viewed on logarithmic scales, the deabsorbed X-ray map and the radio map appear quite similar (Fig. 5). In order to quantify this similarity, we performed a point-by-point comparison between the deabsorbed X-ray image and the most recent (epoch 1994) $\lambda 6$ cm VLA map (Koralesky & Rudnick 1998). The time differences between the radio and X-ray observations (~ 1 year) will have no effect, given that typical proper motions in Cas A are of order $0.1'' \text{ yr}^{-1}$ (Tuffs 1986). Figure 6 shows this correlation for 4'' pixels. This relationship has a correlation coefficient of $r=0.75$, and appears to be real but scatter-dominated.

We can parameterize the relationship between the deabsorbed X-ray surface brightness ($\Sigma_{\text{X ray D}}$) and the radio surface brightness (Σ_{radio}) as

$$\Sigma_{\text{X ray D}} \propto \Sigma_{\text{radio}}^{\eta} . \quad (2)$$

To find the value of η , we performed a least-squares analysis between the quantities $\log(\Sigma_{\text{X ray D}})$ and $\log(\Sigma_{\text{radio}})$. We found the bisector between the two standard least-squares fits, as is appropriate for a scatter dominated linear correlation between two physical quantities (Isobe et al. 1990). At 4'' binning we find a best-fit $\eta = 2.21$ with a corresponding variance of $\sigma_{\eta}^2 = 6.8 \times 10^{-4} = (0.026)^2$. Monte Carlo simulations by Isobe et al. suggest that their formula for finding the variance in the slope underestimates the true uncertainty by about 10%, so we have set our “90% confidence” errors (Table 1) to the 1.8σ level.

We performed two simple tests to show that neither the correlation nor the scatter are artifacts of our analysis. First, to show that the correlation is intrinsic to the data, we rotated one image by 180° about Cas A’s geometrical center before re-correlating the data, whereby the correlation coefficient dropped

from $r=0.75$ to $r=0.41$. This implies that the correlation is due to small scale structure, and is not simply a byproduct of Cas A’s overall circular morphology. Second, to show the reality of the scatter, we created a simulated X-ray map, by assigning to each pixel an X-ray surface brightness that combined the radio surface brightness of that pixel scaled by a power law of 2.21, plus a random term representing the Poisson scatter in the X-ray map. The correlation between the radio and the simulated X-ray image showed no significant scatter, implying that the scatter in figure 6 due to statistical fluctuations is small compared with that observed. Possible physical explanations for this scatter are discussed in §3.2.

We performed the correlation analysis described above on maps with successively larger bin sizes in order to investigate the robustness of our analysis and investigate how increasing the pixel size affects the value of η (Table 1). As the data are binned, the best-fit η decreases, but its maximum value remains at about $\eta_{\text{max}} \approx 2.3$.

To illustrate how smoothing could bias the measured values of η , assume that there exists a value $\eta_o > 1$, such that $\Sigma_{\text{X ray D}} = C \times \Sigma_{\text{radio}}^{\eta_o}$. Thus the averaged quantities would be subject to the inequality:

$$\langle \Sigma_{\text{X ray D}} \rangle = \langle C \times \Sigma_{\text{radio}}^{\eta_o} \rangle \geq C \times \langle \Sigma_{\text{radio}} \rangle^{\eta_o} . \quad (3)$$

One possible explanation for the decreasing η with resolution is that this bias affects both the dim and bright parts of Cas A to about the same degree; however in proportion to their average brightness the dimmer regions are affected to a greater degree, so our logarithmic fitting returns a flatter slope η . Another possibility is that the binning of data lowers the dynamic range of the fit, thus skewing η towards its uncorrelated value of unity. A third possible explanation is that smoothing increases the importance of path-length variations as the governing physical parameter, thus also skewing η towards unity. Regardless of the particular explanation, the trend shown in Table 1 suggests that the intrinsic value of η is between 2.2 and 2.3.

2.4. Deviations from the Trend

Figure 7 is a map of the quantity $\log(\Sigma_{\text{radio}}^{2.21} / \Sigma_{\text{X ray D}})$, or a measure of deviations from the best-fit slope η . Consistent with an overall physical correlation, this map shows very little structure. There are no large scale features such as the shell or the western hot

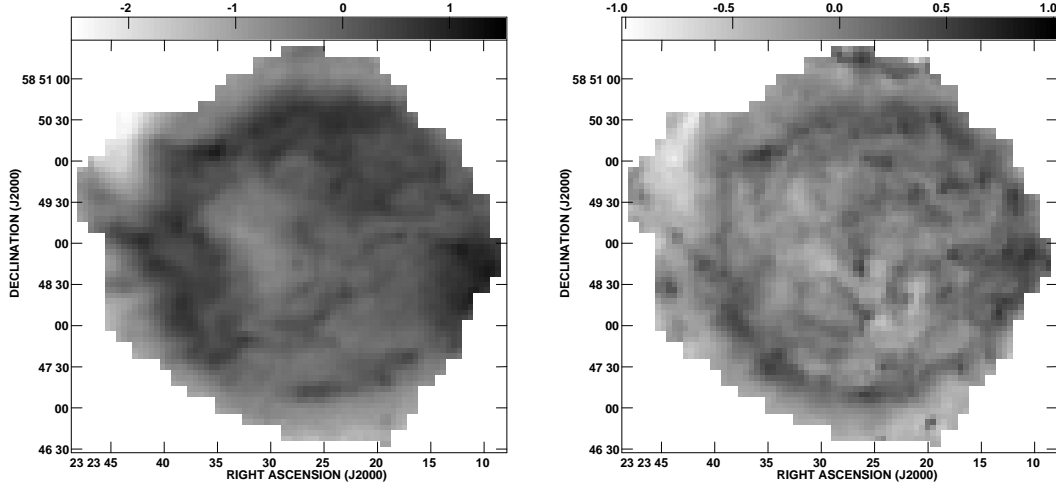


Fig. 5.— Logarithmically scaled images of Cas A. We present, from left to right, the deabsorbed X-ray image and the $\lambda 6$ cm VLA map. The pixel size is $4''$, the same as the beam size. The images are scales to correspond to the axes in Fig 6.

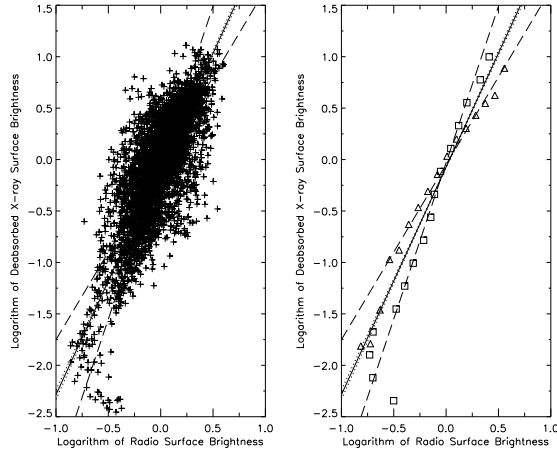


Fig. 6.— Log-log plots correlating the images in Fig 5. The left-hand plot is a standard scatter-plot with 3948 data points. For a majority of points, the random errors are smaller than the symbols plotted. On the right is a plot of the median $\log(\Sigma_{X\text{rayD}})$ in evenly spaced bins of $\log(\Sigma_{\text{radio}})$ (triangles) and visa versa (squares). Both data sets are scaled to units of their respective overall median values. The same lines are plotted on each graph: the dashed lines represent the two standard least-squares fits ($\eta_{xy}=1.7$, $\eta_{yx}=3.0$); the dotted lines represent the 90% confidence range in the slope; and the solid line is the bisector of the two least-squares slopes.

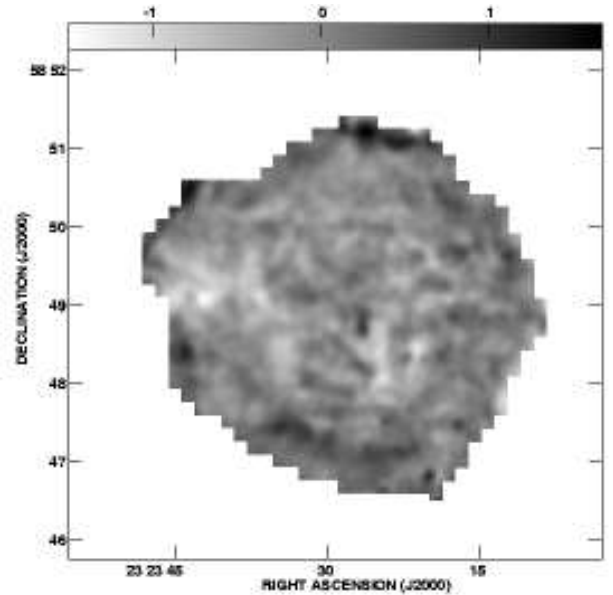


Fig. 7.— Plot of the quantity $\log(\Sigma_{\text{radio}}^{2.21} / \Sigma_{X\text{rayD}})$. The greyscale ranges from $\log(\text{min/mean}) = -1.51$ (white) to $\log(\text{max/mean}) = 1.67$ (black). Like Fig.4, this image is oversampled with a $0.5''$ pixel size, but a resolution of $4''$.

Table 1: The X-ray/radio Regression Parameters

Resolution	N	r	η
4''	3948	0.75	2.21 ± 0.05
8''	876	0.75	2.19 ± 0.11
16''	210	0.76	2.14 ± 0.17
32''	47	0.75	1.96 ± 0.35
64''	10	0.49	1.43 ± 0.72

N = the number of independent points

r = the correlation coefficient

η = the log-log surface brightness slope (see equation 2) with 90% confidence errors

spot. A few key features are present, however. Some are relatively radio bright: the northern knot region; a knot near the center; and the outlying structure in the south. In addition, there is a relatively X-ray bright feature on the eastern shell.

3. Discussion

3.1. Proportionate Partition as a Possible Origin for the Correlation

The main objective of comparing the X-ray and radio emission in Cas A is to identify the physical relationships among the thermal plasma, cosmic ray electrons and magnetic field. In this section we show that our results are consistent with proportionate partition between the energy content of the gas and magnetic field. We also develop a physical justification for this by postulating a turbulent magnetohydrodynamic (MHD) plasma, which we argue is continuously amplifying the magnetic field. As both the trend and the exceptions are real, this scenario should be interpreted as valid “on average,” but not necessarily for each feature in Cas A.

The ROSAT band spectrum of Cas A is dominated by line emission from H and He-like ions of Mg and Si and the L-shell ions of Fe (Holt et al. 1994). Thus by assuming a constant temperature plasma, we can relate the X-ray emissivity* ($\varepsilon_{\text{X-ray}}$) to the gas density (n_{gas}) as:

$$\varepsilon_{\text{X-ray}} \propto n_{\text{gas}}^2 \quad (4)$$

Cas A’s radio emission mechanism is believed to be

*Here the emissivity, $\varepsilon_{\text{X-ray}}$, is defined in an analogous way to the radio emissivity, such that $\Sigma_{\text{X-ray,D}} \propto \int \varepsilon_{\text{X-ray}} dl$, where l is the path length.

synchrotron radiation (Rosenberg 1970), arising from relativistic electrons (of density n_{rel}) interacting with the magnetic field (B). We therefore characterize the radio emissivity ($\varepsilon_{\text{radio}}$) as:

$$\varepsilon_{\text{radio}} \propto n_{\text{rel}} B^{1+\alpha} \quad (5)$$

where α is the radio spectral index ($\alpha = 0.77$, Baars et al. 1977).

Anderson et al. (1994) concluded that the radio brightness of the compact features in Cas A is governed primarily by magnetic field amplification. For this reason, we believe it reasonable to assume a constant (or uncorrelated) relativistic electron density. Therefore, equation 5 becomes:

$$\varepsilon_{\text{radio}} \propto B^{1+\alpha} \quad (6)$$

In their MHD simulations, Jun, Norman, & Stone (1995) show that Rayleigh-Taylor (R-T) instabilities in young SNRs are significantly enhanced by the presence of a magnetic field. Kelvin-Helmholtz instabilities, created by the shear flow along the R-T fingers, greatly enhance the magnetic field — especially on small scales. In addition, MHD studies of simple shear systems show that the magnetic field is amplified quickly as the energy cascades to smaller scales (Malagoli, Bodo, & Rosner 1996). On the scale where the magnetic field becomes dynamically important, reconnection and dissipation occur. It is therefore plausible that the magnetic field in Cas A is being amplified to the point of equipartition with the hot gas, locally on the smallest observable scales, so:

$$\frac{B^2}{8\pi} \approx U_{\text{gas}} \quad (7)$$

In aggregate this is approximately true. If one assumes equipartition between the magnetic field and the relativistic plasma, an energy density for each of these can be derived simply from the overall radio flux density. This overall magnetic energy density ($\frac{B^2}{8\pi}$) is comparable to the thermal energy density (U_{gas}) estimated from the integrated ASCA X-ray spectrum (Allen, G.E. *private communication*).

This suggestion of equipartition is apparently incompatible with the simulation of Jun & Norman (1996), whose 3-D simulations predicted magnetic fields significantly lower than equipartition. However, they also found that the higher the resolution of the simulation (i.e., the lower effective viscosity),

the greater the resultant magnetic field. With regard to the analysis presented here, this distinction is moot. If the turbulent cascade is halted on the smallest scales by the magnetic pressure, the equipartition relation (equation 7) should hold. On the other hand, if the turbulent cascade is the primary amplifier of the magnetic field, but is halted before the magnetic field reaches equipartition, then one would expect the system to still be in proportionate partition, i.e.:

$$B^2 \propto U_{\text{gas}} \propto n_{\text{gas}} \quad (8)$$

The analysis presented here cannot distinguish between equipartition (equation 7) and the looser constraint of proportionate partition (equation 8). Similarly, it does not matter here whether U_{gas} represents the turbulent energy density or the thermal energy density, so long as the energy density scales linearly, on average, with the gas density ($U_{\text{gas}} \propto n_{\text{gas}}$). We now combine equations 4, 6 and 8 to find a relationship between the X-ray and radio emissivities:

$$\varepsilon_{\text{X ray}} \propto B^4 \propto \varepsilon_{\text{radio}}^{\frac{4}{1+\alpha}} \propto \varepsilon_{\text{radio}}^{2.26} \quad (9)$$

This simple relationship agrees remarkably with the value of η found in §2.3.

A similar and independent conclusion about turbulent magnetic field amplification was found by Koralesky & Rudnick (1998), who examined the changes in Cas A's radio emission as a function of azimuth over an 11 year baseline. They found that regions with the largest decrease in fractional polarization (corresponding to a decrease in order of the magnetic field) are decreasing the least in flux density. They suggest that the same process which is randomizing the magnetic field's orientation is also amplifying it, partially compensating for expansion losses.

This relationship between the radio and X-ray surface brightness is very different from the predictions of most other simple models. For example, in an isobaric model, the magnetic pressure and thermal pressure add to a constant, so the surface brightnesses would be anti-correlated. More realistically, a compression scenario where the magnetic field scales inversely with area so $B \propto n_{\text{gas}}^{2/3}$, implies that $\eta = 1.7$, which is also inconsistent with the data. If instead, we make the equally simple assumption that the relativistic electron density is proportional to the thermal gas density ($n_{\text{rel}} \propto n_{\text{gas}}$), then we find $\eta = 2.0$. While we cannot completely rule out this possibility, we do not favor it. The Larmor radii of the relativistic electrons are very

small ($\sim 10^9$ cm for a 1 GeV particle in a 1 mG magnetic field), tightly coupling them to magnetic field lines, which in turn are coupled to the plasma. This suggests that $n_{\text{rel}} \propto n_{\text{gas}}$ may be a good assumption, but then one would also expect a relation between the magnetic field and density. When a magnetic field dependence is included, η is significantly reduced. For example, if $n_{\text{rel}} \propto n_{\text{gas}} \propto B$ then $\eta = 0.7$, which is clearly inconsistent with the correlation.

3.2. Possible Contributions to the Scatter

The simple model that fits the surface brightness ratio rests on three assumptions: constant relativistic electron density, constant X-ray emissivity per density squared ($\varepsilon_{\text{X ray}}/n_{\text{gas}}^2$), and proportionate partition. The relative flatness of the ratio map shows that deviations from these assumptions on large scales are absent. It is plausible, however, that the substantial scatter of the ratio for individual cells from the trend line represents local violation of one or more of these assumptions. The log of the rms deviation about the trend line is ± 0.38 (a factor of ~ 2.5); the log of the maximum excursion is ± 1.5 .

If the scatter is due entirely to variations of n_{rel} or B^2/n_{gas} (proportionate partition), we find the corresponding rms variation of these is ± 0.17 in the log, or a factor of ~ 1.5 . The X-ray emissivity is a function of both gas temperature and metal abundance. The emissivity scales linearly with the abundance of the metals producing the dominant lines in the ROSAT band, namely Mg and Si; thus local rms variations of a factor of ~ 2.5 in metallicity can account for the scatter. The emissivity scales with temperature in a less straightforward way, but deviations of $\log(\varepsilon_{\text{X ray}}/n_{\text{gas}}^2)$ of ± 0.4 can be accounted for by $\log(\text{kT})$ variations of ± 0.4 .

Scatter of the degree indicated in any of these parameters is physically plausible. For instance, small scale gas pressure variations associated with a shock encountering a density enhancement can be as large as a factor of 6 (Dohm-Palmer & Jones 1996), which in turn could produce variations of B^2/n_{gas} or $\varepsilon_{\text{X ray}}/n_{\text{gas}}^2$ within the observed range. Measurements of any of these parameters on small angular scales, at best pose a challenge to current and future instruments, and at worst may be infeasible to measure (e.g., n_{rel}).

4. Conclusion

We have performed a comparison of Cas A's radio and X-ray emission to a limiting resolution of $4''$ (0.07 pc). The strong correlation between radio and X-ray surface brightness can be explained by the scenario that Cas A has "on average" a spatially constant relativistic electron density and proportionate partition on small scales between its thermal and magnetic energy densities, as would be expected from a fully turbulent MHD system.

These results may have important implications for theoretical work. The complex plasma physics of SNRs often must be simplified in order for computer simulations to run in a cost-effective manner. Unfortunately, most often one assumption is spherical or cylindrical symmetry, which is incompatible with turbulent flow. It may be possible, instead, to use the proportionate partition relation suggested by our result, along with some other characteristics of fully turbulent systems, to produce a more realistic first-order description of young, core-collapse, supernova remnants.

We thank Barron Koralesky for kindly providing the $\lambda 6$ cm radio data of Cas A in a digitized form. We also wish to thank Glenn Allen and John Dickel for insightful conversation. This work was supported by NASA.

REFERENCES

- Anderson, M. C., Jones, T. W., Rudnick, L., Tregillis, I. L. & Kang, H. 1994, ApJ, 421, L31
- Arendt, R. G., Dwek, E., Petre, R., Dickel, J. R., Roger, R. S., Milne, D. K., & Kesteven, M. J. 1990, ApJ, 350, 266
- Baars, J. W. M., Genzel, R., Pauliny-toth, I. I. K. & Witzel, A. 1977, A&A, 61, 99
- Bieging, J. H., & Crutcher, R. M. 1986, ApJ, 310, 853
- Dickel, J. R., Murray, S. S., Morris, J., & Wells, D. C. 1982, ApJ, 257, 145
- Dohm-Palmer, R. C., & Jones, T. W. 1996, ApJ, 471, 279
- Dyer, K. K., & Reynolds, S. P. 1998, *in preparation*
- Holt, S. S., Gotthelf, E. V., Tsunemi, H. & Negoro, H. 1994, PASJ, 46, L151
- Isobe, T., Feigelson, E. D., Akritas, M. G. & Babu, G. J. 1990, ApJ, 364, 104
- Jun, B. I., Norman, M. L., & Stone, J. M. 1995, ApJ, 453, 332
- Jun, B. I., & Norman, M. L. 1996, ApJ, 472, 245
- Keohane, J. W., Rudnick, L. & Anderson, M. C. 1996, ApJ, 466, 309
- Koralesky, B. T., & Rudnick, L. 1998, *in preparation*
- Lucy, L. B. 1974, AJ, 79, 745
- Malagoli, A., Bodo, G. & Rosner, R. 1996, ApJ, 456, 708
- Matsui, Y., Long, K. S., Dickel, J. R., & Greisen, E. W. 1984, ApJ, 287, 295
- Richardson, W. H. 1972, J. Opt Soc Am, 62, 55
- Rosenberg, I. 1970, MNRAS, 151, 109
- Schwarz, U. J., Goss, W. M. & Kalberla, P. M. W. 1997, A&AS, 123, 43
- Tuffs, R. J. 1986, MNRAS, 219, 13

This 2-column preprint was prepared with the AAS L^AT_EX macros v4.0.